

Check for updates

# Open and Close-Packed, Shape-Engineered Polygonal Nanoparticle Metamolecules with Tailorable Fano Resonances

Yi-Yu Cai, Asma Fallah, Shengsong Yang, Yun Chang Choi, Jun Xu, Aaron Stein, James M. Kikkawa, Christopher B. Murray, Nader Engheta, and Cherie R. Kagan\*

A top-down lithographic patterning and deposition process is reported for producing nanoparticles (NPs) with well-defined sizes, shapes, and compositions that are often not accessible by wet-chemical synthetic methods. These NPs are ligated and harvested from the substrate surface to prepare colloidal NP dispersions. Using a template-assisted assembly technique, fabricated NPs are driven by capillary forces to assemble into sizeand shape-engineered templates and organize into open or close-packed multi-NP structures or NP metamolecules. The sizes and shapes of the NPs and of the templates control the NP number, coordination, interparticle gap size, disorder, and location of defects such as voids in the NP metamolecules. The plasmonic resonances of polygonal-shaped Au NPs are exploited to correlate the structure and optical properties of assembled NP metamolecules. Comparing open and close-packed architectures highlights that introduction of a center NP to form close-packed assemblies supports collective interactions, altering magnetic optical modes and multipolar interactions in Fano resonances. Decreasing the distance between NPs strengthens the plasmonic coupling, and the structural symmetries of the NP metamolecules determine the orientation-dependent scattering response.

1. Introduction

Nanoparticles (NPs) are prized for their composition-, size-, and shape-dependent optical, electrical, and magnetic properties. [1-4]

NPs are often referred to as artificial atoms. as they are building blocks of assembled NP metamolecules and materials, in which interparticle coupling, in analogy to "bonds", controls their structure-function relationships.<sup>[5]</sup> Chemical synthesis produces NPs, in general, with excellent control of composition, size, and shape;<sup>[6]</sup> however some NP compositions and shapes remain hard to prepare. Bottom-up assembly is used to prepare large-area, ordered NP superlattices, driven by interparticle van der Waals, electrostatic, and entropic forces, etc.[7,8] The shape of NPs can create directional bonds in maximizing system entropy by favoring facet-aligned, locally dense NP packings.[9]

However, the deterministic positioning and assembly of small numbers of NPs, also described as NP metamolecules, is more challenging.<sup>[10]</sup> Top-down lithography and deposition of materials are used to create nanostructures on surfaces with arbitrary design.<sup>[11,12]</sup> However, top-down

patterning of nanostructures with ultrafine gaps is very difficult, especially to scale over large numbers of nanostructures.<sup>[13,14]</sup> NP metamolecules can be assembled from the bottom up through directional interactions between colloidal NPs, such as

Y.-Y. Cai, A. Fallah, J. Xu, N. Engheta, C. R. Kagan Department of Electrical and Systems Engineering University of Pennsylvania Philadelphia, PA 19104, USA E-mail: kagan@seas.upenn.edu S. Yang, Y. C. Choi, C. B. Murray, C. R. Kagan Department of Chemistry University of Pennsylvania Philadelphia, PA 19104, USA A. Stein Center for Functional Nanomaterials Brookhaven National Laboratory Upton, NY 11973, USA

J. M. Kikkawa, N. Engheta
Department of Physics and Astronomy
University of Pennsylvania
Philadelphia, PA 19104, USA
C. B. Murray, N. Engheta, C. R. Kagan
Department of Materials Science and Engineering
University of Pennsylvania
Philadelphia, PA 19104, USA
N. Engheta
Department of Bioengineering
University of Pennsylvania
Philadelphia, PA 19104, USA

(D

The ORCID identification number(s) for the author(s) of this article can be found under https://doi.org/10.1002/adma.202301323

DOI: 10.1002/adma.202301323

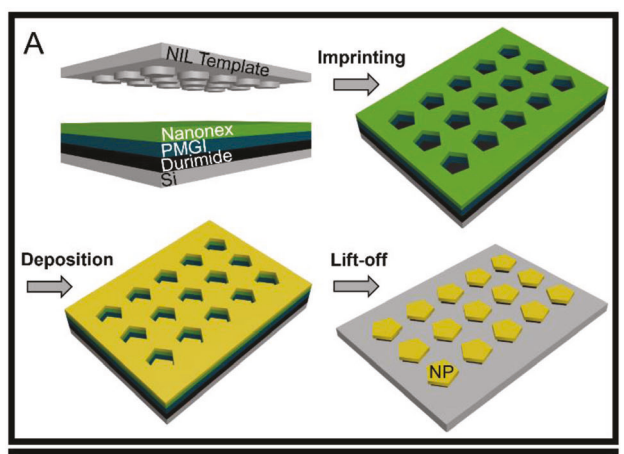
15214055, 2023, 33, Downloaded from https://onlinelibrary.wiley.com/doi/10.1002/adma.2023.0323 by University Of Pennsylvania, Wiley Online Library on [19/03/2024]. See the Terms and Conditions (https://onlinelibrary.wiley.com/terms-and-conditions) on Wiley Online Library for rules of use; O A articles are governed by the applicable Centure Commons

hydrogen bonding between DNA $^{[15]}$  or polymer ligands, $^{[16]}$  or directed by external fields, using methods that include optical printing, electrostatic assembly, electrophoretic deposition, magnetic-field-directed self-assembly, etc. $^{[17]}$  To spatially pattern NPs on substrates, topographical templates differentiating the design locations are often employed. $^{[18]}$ 

Template-assisted self-assembly is a highly scalable, hybrid method for positioning colloidal NPs with the precision of lithography.[19-22] One widely used method is capillary assembly, in which a NP dispersion is deposited between a glass slide and a substrate patterned with size- and shape-engineered trap sites.<sup>[23]</sup> NPs accumulate near the meniscus at the three-phase contact line, and as the glass slide is translated with respect to the substrate, the meniscus moves across the substrate surface. Capillary forces, that is the elastic restoring forces created by distortion of the pinned meniscus, dominate over other interparticle forces and drive the NPs to fill the trap sites.[24] Without strong directional interparticle forces, template geometry and confinement are more important for creating complex structures and have been exploited to deterministically assemble single NPs, NP dimers, and a limited number of open and close-packed NP metamolecules from mostly spherical or rod-shaped NPs, [25-28] with few other example shapes. [29,30] Self-assembly of fabricated, more complex-shaped polyhedral particles has been investigated in the um particle size regime.[12,31,32]

Monodisperse polygonal NPs are excellent building blocks for studying the relationship between the shape of NPs and the shape of templates in directing the assembly. Here, we develop a method using nanoimprint lithography to scalably produce polygonal NPs, which have square, pentagonal, and hexagonal shapes. The NPs can be composed of a variety of materials (e.g., Pd, Ge, Au) attainable through the physical deposition of thin films. Using the template-assisted self-assembly method, we assemble polygonal NPs into open or close-packed structures with controlled numbers of NPs. The geometry of the templates defines the organization of the NP metamolecules and the interparticle distances, to inter-NP distances even <10 nm. The polygonal shapes of the NPs determine the coordination number and spatial symmetry of the NP metamolecules.

We focus the study on polygonal Au NPs as a materials basis set as it allows studies of NP metamolecule structure and its correlation with optical properties. In analogy to electronic coupling in molecules, collective plasmonic resonances in metamolecules depend on the number, interparticle distances, and shape-directed coordination of NPs.[5] We construct cyclic and polycyclic plasmonic NP metamolecules from polygonal NPs. Circulating displacement currents generate magnetic optical modes that interfere with collective super radiant modes, leading to the formation of Fano resonances.[33-37] The central NP in the assembly plays a crucial role in these collective interactions and sculpts the resonances. By modifying the distance between NPs and manipulating the higherorder sub radiant modes within the metamolecules, we can tune the Fano resonances. The symmetry of the NP metamolecule structure also determines its orientation-dependent scattering response.



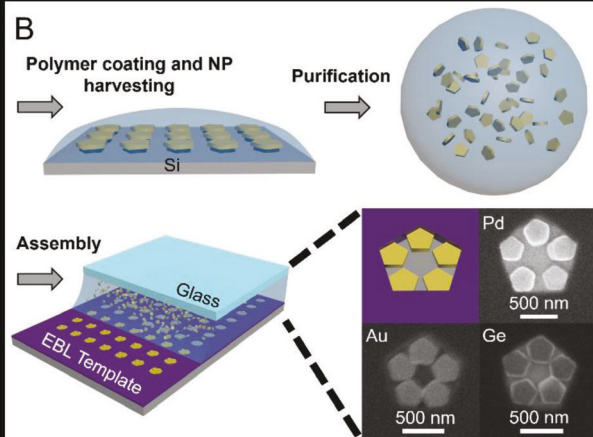


**Figure 1.** A) Schematic of NP fabrication. Polygonal molds are imprinted into thermal resist (green) and undercut layers (blue) are developed. Material (gold) is deposited and the resist and material atop the resist are lifted off and treated with  $O_2$  plasma to form NPs anchored by a sacrificial layer (black) to the substrate surface. B) Schematic of NP dispersion and assembly. NPs are simultaneously coated with polymer ligands and harvested from the substrate surface, by immersing samples in ligand solutions, to form colloidal dispersions. The NP dispersions are purified by centrifugation and redispersion in solvents to remove excess polymer ligands and ultimately form aqueous dispersions. A capillary-driven, template-assisted assembly process is used to assemble NPs from their aqueous dispersions in resist templates (purple) to form NP metamolecules. Right: SEM images of cyclic pentamers of pentagonal Pd, Ge, and Au NPs.

## 2. Results and Discussion

We prepare square, pentagonal, and hexagonal NPs using nanoimprint lithography and thermal evaporation of thin films (Figure 1A). Details are in the Experimental Section. Briefly, we use e-beam lithography (EBL) to define 10 mm  $\times$  10 mm imprint molds in which the side lengths of the polygons are fixed to 200 nm and the pitch of the polygons is set to 600 nm (square and pentagon) or 800 nm (hexagon) (Figure S1A–C, Supporting Information). We use a trilayer resist design, including thermal imprint, undercut, and sacrificial layers.  $^{[38]}$  The templates are imprinted into the thermal resist and the undercut layer is developed. Thin films,  $\approx 30–50$  nm in thickness are deposited by

15214055, 2023, 33. Downloaded from https://onlinelibrary.wiley.com/do/10.1002/adma.202313123 by University Of Pennsylvania, Wiley Online Library on [19/03/2024]. See the Terms and Conditions (https://onlinelibrary.wiley.com/erms-and-conditions) on Wiley Online Library for rules of use; OA articles are governed by the applicable Cerative Commons

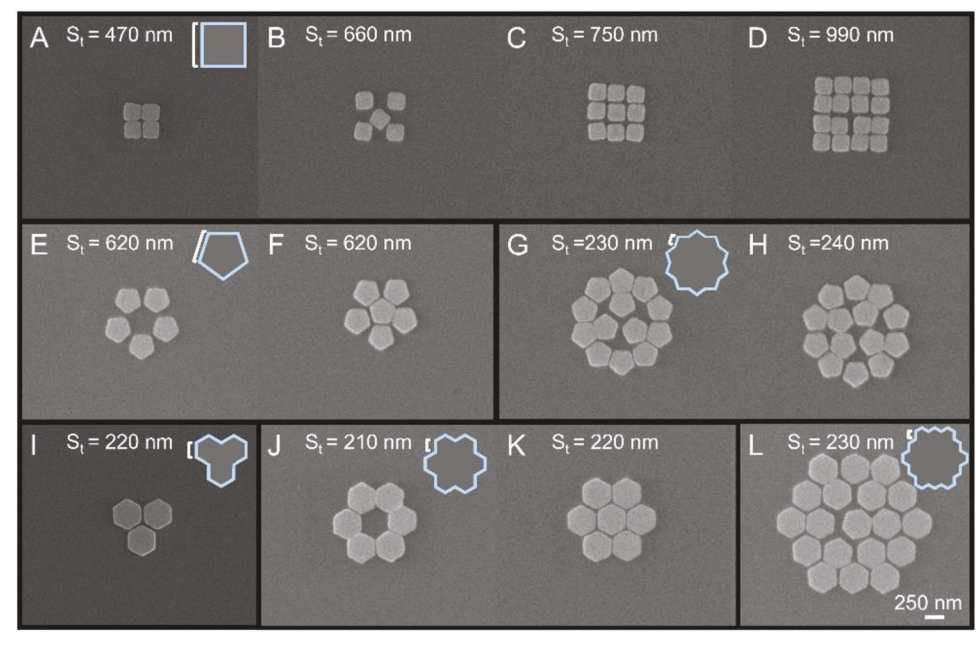


Figure 2. A–L) SEM images of assemblies of four (A), five (B), nine (C), and sixteen (D) square; five (E), six (F), thirteen (G), and fourteen (H) pentagonal; and three (I), six (J), seven (K), and nineteen (L) hexagonal Au NP metamolecules after removing the EBL template. The inset is the design of the size-and shape-engineered templates labeled with S<sub>1</sub>. Templates with the same design shape are grouped within a black frame.

thermal evaporation. Lift-off and O $_2$  plasma etching is used to remove the resist and deposited film atop the resist, creating arrays of polygonal-shaped NPs anchored by the sacrificial layer to the substrate surface (Figure S1D–F, Supporting Information). One imprint cycle produces  $\approx 10^8$  NPs with side length,  $S_{\rm NP}$ , of 225  $\pm$  6 nm (square), 217  $\pm$  4 nm (pentagon), and 213  $\pm$  4 nm (hexagon), analyzed from scanning electron microscopy (SEM) images of >90 NPs from two NP batches for each shape.  $S_{\rm NP}$  is slightly expanded from that of the templates after development (Figure S2, Supporting Information). Transmission electron microscopy (TEM) and atomic force microscopy (AFM) images show the polycrystalline nature and flatness of the polygonal NPs, with surface roughness <5 nm (Figures S3 and S4, Supporting Information).

NPs are coated with polymer ligands to stabilize them in solvent and simultaneously are harvested from the substrate surface by dissolving the bottom sacrificial resist layer through soaking and sonicating the samples in solutions of the polymer ligands in N-methyl-2-pyrrolidone (NMP) (Figure 1B). Excess ligand is removed through a purification process of sequential centrifugation and redispersion in solvents. Each batch of  $\approx 10^8$  NPs is concentrated in <5 µL water for use in assembly. NPs are assembled via template-assisted, capillary self-assembly in resist templates defined by EBL (Figure S5, Supporting Information). After the assembly process, the EBL resist template is lifted off. Our approach is generalizable to the fabrication and assembly of different compositions of size- and shape-tailored NPs, which we show by example for Pd, Ge, and Au pentagonal NPs assembled in pentagonal templates to form cyclic pentamer NP assemblies (Figure 1B). In the remainder of the paper, we focus on Au NPs coated with thiolated-poly(vinylpyrrolidone) (PVP) ligands[39] as they support plasmonic resonances allowing us to correlate the structure and optical properties of NP metamolecules.

In the template-assisted assembly of NP metamolecules, the shape, and side length  $(S_i)$  of the templates define the number and organization of NPs in metamolecules, while the shape of the NPs determine their coordination number. Figure 2 shows representative SEM images of assembled Au NP metamolecules. We develop design rules for NP metamolecules by matching the size and shape of the templates to that of the perimeter of a targeted NP oligomer to guide the assembly of open and close-packed nmembered NP metamolecules. For example, we assemble closepacked,  $n \times n$  arrays of square Au NPs in square templates, where n = 2, 3, 4 forms four, nine, and 16 NP metamolecules (Figure 2A,C,D).  $S_t$  of the square templates satisfy the equation  $S_t$ =  $n \times S_{NP}$  +  $(n-1) \times g1$  +  $2 \times g2$  nm (Figure 2A,C,D) to have nonoverlapping edges with interparticle gaps, g1, and NP-template gaps, g2. g2 is typically <5 nm as NPs are brought close to the EBL-resist template walls or corners by capillary forces created by drying of the solvent in the template traps. The four-fold symmetry of the square leads to a coordination number of NPs of four in the inner shell (Figure 2C,D). g1 for the examples in Figure 2A,C,D are ≤40 nm, and can be <10 nm in some cases as shown in Figure S6 (Supporting Information). g1 increases as  $S_{t}$  is increased. For  $S_{t}$  between that for n = 2 and 3 and for a large enough central void, the assembly is frustrated and a rotated, center-square NP inclusion fits between the four corner square NPs (Figure 2B). As S<sub>+</sub> is further increased, NPs can assemble to form square annuli, until S, is large enough that an additional square NP fits in the central void (Figure 2B,C). Largerarea SEM images of Au NP assemblies in size-tailored, squareshaped templates are shown in Figure S7A-F (Supporting Information). Non-regular polygons, such as square "Greek" crossshaped assemblies are demonstrated by choosing similar shaped templates (Figure S7G,H, Supporting Information).

15214095, 2023, 33, Downloaded from https://onlinelibrary.wiley.com/doi/10.1002/adma.202301323 by University Of Pennsylvania, Wiley Online Library on [19/03/2024]. See the Terms and Condition of the Condition o

s (https://onlinelibrary.wiley.com/terms-and-conditions) on Wiley Online Library for rules of use; OA articles are governed by the applicable Creative Commons

The assembly of pentagonal NPs is less explored, since the shape is not readily accessible synthetically. Figure 2E-H shows pentagonal Au NP metamolecules. The pentagonal NP metamolecules adopt Penrose pentagonal tilings, [40] including hexamers with pentagonal-shaped exteriors and a five-coordinated center NP (Figure 2F), and tridecamers with a ten-NP annulus and a three-NP, decagonal-shaped inner space (Figure 2G). The critical value determining whether a center-NP is accepted to form a hexamer is when  $S_t$  is  $\approx 2 \times S_{NP} \times (1 + \cos 72^\circ) + 2 \times 10^{-5}$ g2/tan54° nm (Figure S8, Supporting Information). Below such a value, open structures composed of NPs with overlapping edges are assembled in an annulus with a central void smaller than a NP (Figure S9A, Supporting Information). Increasing S<sub>+</sub> to lengths greater than the critical dimension for hexamer formation results in larger interparticle gaps (Figure S9B-D, Supporting Information), and a higher yield of close-packed structures. However, the kinetic nature of the capillary assembly process<sup>[24,41]</sup> and the stronger capillary interaction of NPs with the template walls<sup>[42]</sup> can form open NP annuli with central voids larger than a single NP, for example, the cyclic pentamer of pentagonal (Figure 2E), cyclic octamer of square (Figure S7C, Supporting Information), and cyclic hexamer of hexagonal (Figure S10B, Supporting Information) Au NPs. As indicated by previous research<sup>[24]</sup> the capillary assembly process may involve a series of sequential stages, with NPs potentially forming open or close-packed structures at distinct time steps, which warrants further investigation. For larger n-membered NP assemblies, an increase in S, results in larger interparticle gaps and/or more NPs in a single trap, as exemplified by pentagonal NP tridecamers and tetradecamers in Figure 2G,H.

Similarly, by controlling the shape of the template to be structured around the sides of the NPs, and the size  $S_{\rm t}$  of the template to be just smaller or larger than  $S_{\rm NP}$ , hexagonal Au NPs with sixfold symmetry are assembled into trimers, hexamers, heptamers, and nonadecamers (Figure 2I–L; Figure S10, Supporting Information). The heptamers and nonadecamers have a complete NP annulus and six-coordinate hexagonal NPs in the inner shell. Larger templates lead to more possible configurations of defects, as demonstrated by hexagonal Au NP penta- to nona-decamers (Figure S10C, Supporting Information).

Across 1 mm² templated areas, regional variations in NP concentration due to solvent evaporation and fluctuations in chamber conditions may cause nonspecific deposition of large random NP aggregates and non-uniform yields across the patterned wafer (Figure S11A, Supporting Information). [43] In 2500  $\mu$ m² templated areas, yields of n-membered NP metamolecules with n < 10 are >25% and increase as n decreases, in agreement with a previous study on template-assisted, capillary self-assembly of wet-chemically synthesized, spherical Au NP metamolecules (Figure S11B, Supporting Information). [25] n > 10 yields drop <10%.

We characterize the optical properties of the Au NP metamolecules using dark-field scattering spectroscopy. <sup>[25,26]</sup> The elevation angle of the incident white light is  $\approx 10^{\circ}$  above the horizontal. By rotating a linear polarizer, we choose the s-polarized excitation to probe the scattering signal to be in the plane of the NP metamolecules, and thus to measure the structure-dependent, optical responses characteristic of cooperative interactions between NPs (Figure S12A, Supporting Information). Representa-

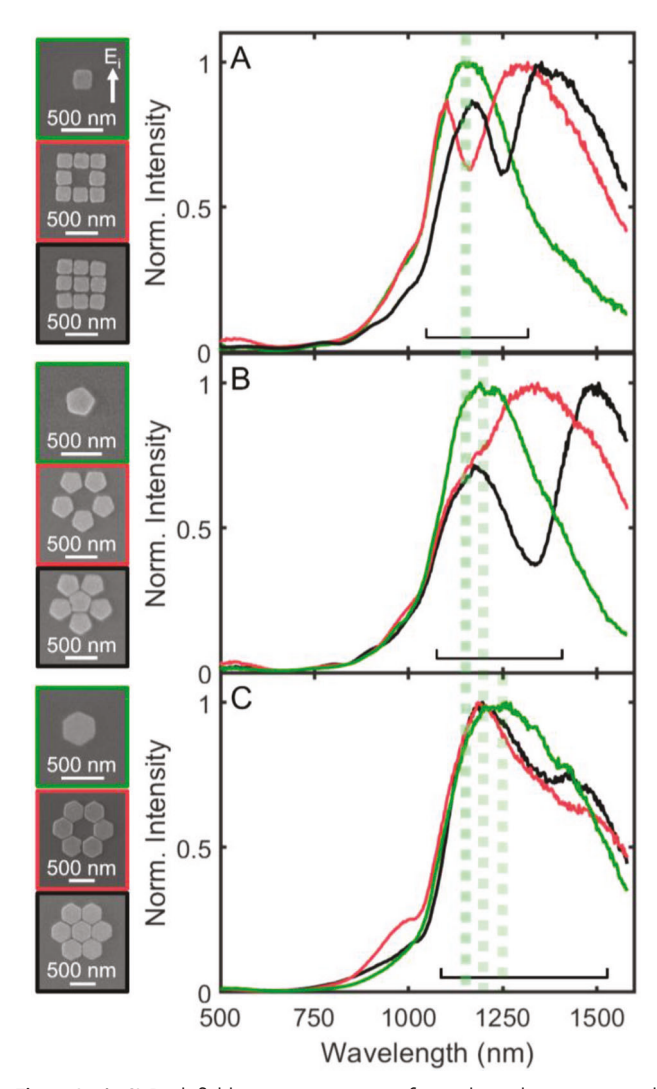


**Figure 3.** A–C) Dark-field scattering spectra of a single, cyclic octamer, and polycyclic nonamer of square Au NPs (A); a single, cyclic pentamer, and polycyclic hexamer of pentagonal Au NPs (B); and a single, cyclic hexamer, and polycyclic heptamer of hexagonal Au NPs (C). Spectra are plotted with colors corresponding to the borders of the SEM images of the measured NP metamolecules shown on the left, and the s-polarization of incident light is marked in the top left image of (A). The green dashed lines mark the peaks of single square, pentagonal, and hexagonal NPs. The full width half maximum of the single NP is marked by a range bar in the bottom of each plot.

tive scattering spectra are plotted in **Figure 3**. For single square, pentagonal, and hexagonal Au NPs, the effective plasmon lengths are 225, 334, and 426 nm,  $^{[44]}$  and thus the resonance energies redshift from  $\approx\!1150$  to 1200 and 1250 nm. Simulated single-particle scattering cross-sections follow the same trend and confirm the dipolar character of the resonances (Figure S12B, Supporting Information).

We focus the study on comparing the scattering spectra of open and close-packed NP assemblies with one complete annulus, which support more resolvable resonances than assemblies with larger numbers of NPs and multiple annuli. In analogy to molecules, we describe these open and close-packed assemblies

15214095, 2023, 33, Downloaded from https://onlinelibrary.wiley.com/doi/10.1002/adma.202301323 by University Of Pennsylvania, Wiley Online Library on [19/03/2024]. See the Terms and Conditions (https://onlinelibrary.wiley.com/terms

nditions) on Wiley Online Library for rules of use; OA articles are governed by the applicable Creative Commons

as cyclic and polycyclic NP metamolecules. The spectra of squareshaped, cyclic octamer and polycyclic nonamer metamolecules constructed from square NPs have scattering spectra that extend from the blue side and beyond the red side of the single square NP spectrum, with intermediate dips unseen in the single particle spectrum (Figure 3A). Pentagonal Au NPs are used to construct pentagonal-shaped, cyclic pentamers and polycyclic hexamers, which similarly have scattering spectra broader than that of the single pentagonal NP spectrum. However, while the spectrum of the polycyclic hexamer shows an obvious spectral dip, the cyclic pentamer does not (Figure 3B; Figure S13, Supporting Information). The contrast suggests that there are differences in the collective plasmonic modes when coordination number is varied. The linewidth of the single hexagonal Au NP (0.33 eV), compared to that of the square (0.22 eV) and pentagonal NP (0.27 eV), is so broad that differences in the scattering spectra of cyclic hexamers and polycyclic heptamers are almost indistinguishable from each other and that of the single hexagonal NP (Figure 3C). The comparison between polygonal NP metamolecules emphasizes the importance of NP shape in defining the spectral linewidth of the constituents NPs and the shape-directed coordination number that controls the coupling between NPs and thus the scattering response of NP metamolecules.

The dark-field scattering spectra of a square-shaped cyclic octamer and polycyclic nonamer constructed from square Au NPs, made using templates with the same  $S_t$  and with interparticle gaps of  $\approx$ 40 nm, are plotted in **Figure 4**A,B. Orientations of the metamolecules are rotated clockwise by  $0^{\circ}$ ,  $15^{\circ}$ ,  $30^{\circ}$ , and  $45^{\circ}$  from the configuration shown in the SEM image. The optical excitation remains incident from the right, and the corresponding spectra are plotted with black, red, green, and blue colors. Optical magnetic resonances are anticipated in the scattering spectra of the cyclic octamer and polycyclic nonamer, given their cyclic character. The magnetic resonances are detected at  $\lambda > 1000$  nm after filtering out the electric dipole mode with a cross-polarizer in the detection path (Figure S14, Supporting Information). [46]

At 0° sample rotation, the scattering of the cyclic octamer has a long wavelength peak centered at 1290 nm (labeled I), a dip centered at 1160 nm (II), and a short wavelength scattering peak centered at 1100 nm (III) (Figure 4A). As the rotation angle of the cyclic octamer is increased, scattering peak III is dampened and spectral dip II finally disappears at a 45° rotation. The same 45° sample rotation does not change the scattering from single square Au NPs (Figure S15, Supporting Information). For the polycyclic nonamer, peaks I and III and dip II are centered at 1360 (I), 1250 (II), and 1180 nm (III), respectively. In comparison to the cyclic octamer, the spectral features for 0° rotation are to the red of that of the cyclic octamer, and interestingly, the spectral dip II of the square Au NP nonamer survives rotation to all angles (Figure 4B), in contrast to that of the cyclic octamer. These trends are reproduced in measurements of other cyclic octamer and polycyclic nonamer NP metamolecules (Figure S16, Supporting Information). The scattering spectra are also measured with a 15° increment in azimuthal angles for a complete 360° clockwise sample rotation, plotted in Figure 4C,D. Peak III at 0° rotation of the octamer disappears at 45° and every 90° increment. In contrast, peak III at 0° rotation of the square nonamer persists at all angles and is maximized at 45° and every

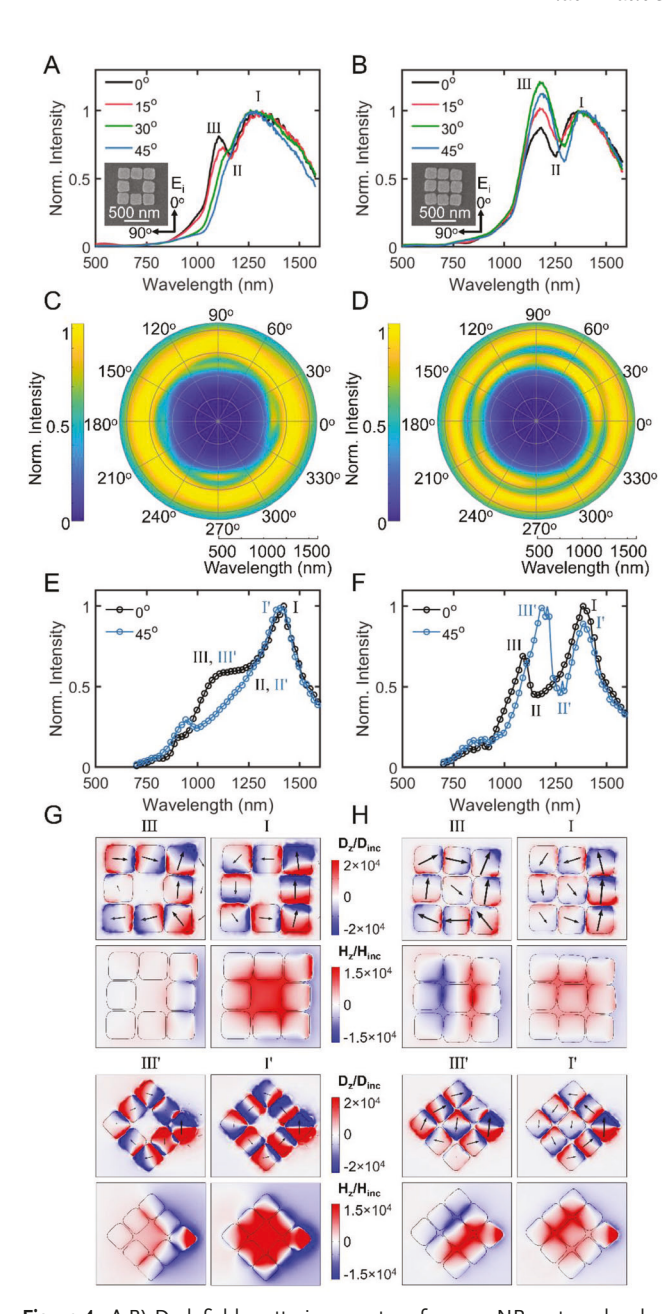


Figure 4. A,B) Dark-field scattering spectra of square NP metamolecules forming a square-shaped cyclic octamer (A) and polycyclic nonamer (B), measured at 0°, 15°, 30°, and 45° clockwise rotation from the configuration shown in the SEM images. Inset: the electric field  $E_i$  of the incident excitation at 0° and 90° sample rotation. C,D) The scattering spectra of the octamer (C) and nonamer (D) are measured at angles of clockwise rotation. The radial direction is the wavelength, and polar angles are the azimuthal angles of sample rotation. Measurements are taken in 15° increments, and values at intermediate angles are obtained through interpolation. Simulated scattering cross-sections at  $0^{\circ}$  and  $45^{\circ}$  clockwise rotation for the structures in (A,B) is plotted in (E,F), respectively. G,H) Simulated time snapshots of the z-component (normal to the sample) of the electric displacement field maps, with electric displacement vectors in the x-y plane overlaid, and magnetic field intensity maps at the peak wavelengths indicated by the labels I and III at 0° rotation, and I' and III' at 45° rotation. The electric displacement field and magnetic field intensity maps are normalized to the incident field and plotted with fixed ranges, allowing for direct comparisons.

1521495-2023, 33. Downloaded from https://onlinelibrary.wiley.com/doi/10.1002/adma.20231323 by University of Pennsylvania, Wiley Online Library on [19/03/2024]. See the Terms and Conditions (https://onlinelibrary.vi.ety.com/terms-and-conditions) on Wiley Online Library for rules of use; OA articles are governed by the applicable Creative Commons is

90° increment. In both cases, the intensities show four lobes in the azimuthal maps, in agreement with their four-fold metamolecule symmetries, while some deviations in relative intensities are anticipated to arise from small structural variations in the assemblies.

Using the same structure and excitation of the square Au NP octamer and nonamer in Figure 4A,B, the scattering cross-sections at 0° and 45° rotation angles of the NP metamolecules are simulated using COMSOL Multiphysics<sup>[47]</sup> and plotted in Figure 4E,F. At 45° rotation, the long wavelength peak, the dip, and the short wavelength peak are labeled with I', II', and III', respectively. The simulated spectra reproduce the experimentally observed trends. The spectral dip disappears in the octamer but remains for the nonamer after a 45° rotation. The differences between the experimental and simulated scattering spectra in relative intensities and resonance energies are anticipated to be caused by discrepancies in the Au dielectric function and in the geometries (i.e., size, shape, roughness) of NPs between experiment and simulation.

In Figure 4G,H and Figures S17 and S18 (Supporting Information), normal components of the electric displacement (D) associated with surface charge densities and the magnetic field (H) are plotted for the peaks and dips labeled in Figure 4E,F for the cyclic octamer and polycyclic nonamer. Time snapshots of D and H normal to the sample with different signs and magnitudes are mapped with shades of red and blue, and the instantaneous spatial distribution of the electric displacement vectors in the x-y plane is represented with arrows. At peaks I and I', the head-to-tail arrangement of electric displacement vectors creates circulating displacement currents that support optical magnetic modes. [48,49] These optical magnetic modes have magnetic fields normal to the oligomer plane, as indicated by the red color in the magnetic field maps. The central NP in the nonamer bifurcates the circular loop, partitioning the electric dipole strength, and creating a weaker magnetic field in the center of the assembly compared to that of the octamer. Magnetic modes are usually sub radiant because of the net-zero electric dipole moment. However, peak I is excited due to symmetry breaking of the metamolecules, because of small variations in their order, and retardation effects, [26,50] which are significant because of our 10° glancing angle illumination and the  $>\lambda/10$  NP size.<sup>[51]</sup> The retardation effects increase the strength of the dipoles on the right side of the metamolecules, as seen by the larger arrows representing the electric displacement vectors.

Peak III for the octamer and nonamer have a net electric dipole moment, as indicated by the simulation in Figure S19 (Supporting Information), and can be seen by summing the electric displacement vectors in Figure 4G,H, and are thus electrically bright but magnetically dark. At 0° rotation (Figure S19, Supporting Information), the central NP in the nonamer strengthens the electric dipole mode compared to the magnetic dipole mode, making peak III strong; whereas for the octamer, the electric dipole mode is not as strong as that of the magnetic dipole mode and peak III is spectrally weak. At 45° rotation, relative to the strength of the magnetic dipole mode, the electric dipole mode of the octamer weakens, while the central NP in the nonamer strengthens the electric dipole mode, consistent with peak III in the octamer vanishing and in the nonamer strengthening. The magnetic field maps show regions of opposite polarity, seen by red and blue col-

ors, marking out-of-phase magnetic moments (Figure 4G,H)<sup>[35]</sup> and the magnetic dipole moments in both oligomers are small in this spectral region (Figure S19, Supporting Information).

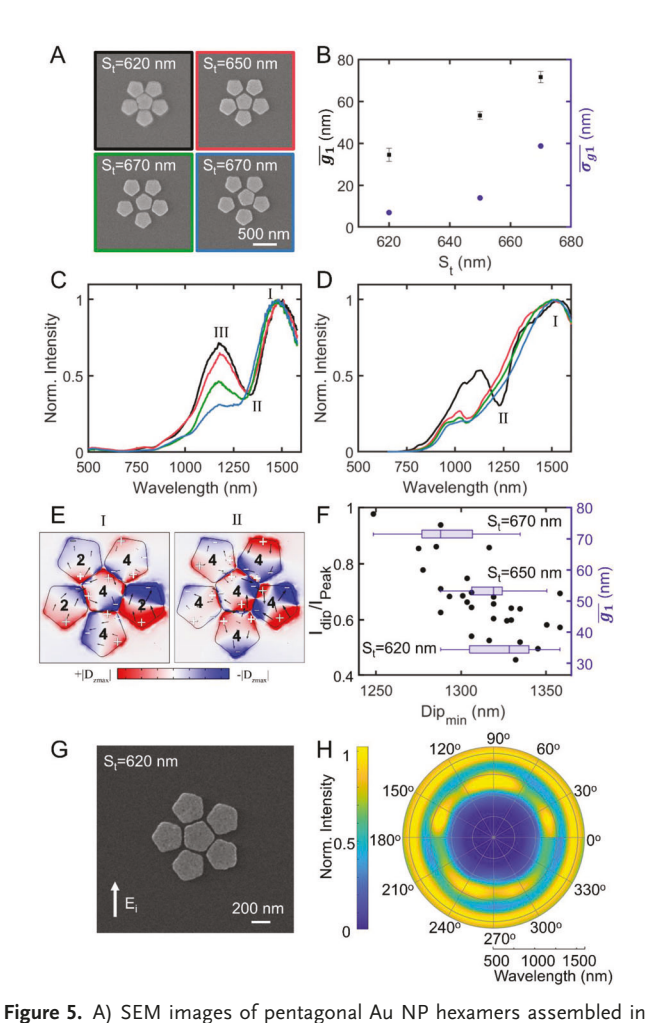
The experimentally observed spectral dips II in Figure 4A,B originate from Fano resonances formed by coupling between the narrow, sub radiant (magnetic) mode, peak I, and a broadband, super radiant (electric) mode, peak III. The simulated radiation from electric and magnetic dipoles supports this interpretation (Figure S19, Supporting Information). At the spectral dips II for the octamer and nonamer at both 0° and 45° rotation, the coupling between peaks I and III is seen as the electric dipole moments no longer complete circulating currents, and thus the magnetic moments are weakened (Figure 4G,H; Figures S17 and S18, Supporting Information).

The  $S_{t}$  of the templates controls the size of the interparticle gap, g1, akin to "bond length". Figure 5A shows SEM images of four representative pentagonal Au NP hexamers assembled in templates with three different S, values, as labeled. Statistical studies of 29 pentagonal Au NP hexamers are plotted in Figure 5B, showing that the average interparticle distance, g1, and standard deviation,  $\sigma_{g1}$ , between the central and the surrounding NPs increases from 34  $\pm$  7 to 53  $\pm$  14 and to 71  $\pm$ 39 nm when S<sub>+</sub> is increased from 620 to 650 and 670 nm, respectively. Larger S, gives more space for the center NPs to explore, thus increasing  $\sigma_{g1}$  and the degree of metamolecule asymmetry. Similar observations are made on nonamers of square NPs and heptamers of hexagonal Au NPs (Figure S20, Supporting Information). In contrast, although a larger S, allows for a higher rotation angle of the NPs, the variation in orientation of the NPs does not change significantly (<5° on average) with increased  $S_t$ , likely because the strong interaction of the NPs in the annulus with the template side walls anchors their orientation, and thus that of the central NPs (Figures S20 and S21, Supporting Information).

The "bond length" governed by S<sub>+</sub> controls the interparticle coupling, thus sculpting the Fano response. The dark-field scattering spectra of four representative pentagonal Au NP hexamer metamolecules are plotted in Figure 5C, with the colors corresponding to the border of their SEM images in Figure 5A. The spectra show two resonance peaks at ≈1500 nm (labeled I) and 1170 nm (III) and a spectral dip in between (II). When S, increases from 620 to 670 nm, larger g1 and higher degrees of asymmetry decrease the coupling strength and the contrast between the intensity of spectral dip II and of peak I, which we describe by  $I_{
m dip}/I_{
m peak}.$  Simulated spectra of the four hexamer metamolecules, plotted in Figure 5D, reproduce the same trend in the modulation of  $I_{\rm dip}/I_{\rm peak}$ . To resolve the modes, we simulate the electric displacement at the pentagonal NP hexamer's spectral peaks and dip (peak I and dip II in Figure 5E, peak III in Figure S22A, Supporting Information) for the metamolecule in Figure 5A with the smallest  $S_{+} = 620 \text{ nm}$ . Peak I and III have net dipole moments from the dipolar charge distribution of constituent NPs, and thus are bright in scattering. In contrast, all the NPs have quadrupolar charge distributions in the dip, consistent with a sub radiant mode causing the Fano interference.<sup>[52]</sup> The magnetic field maps at the three energies show magnetic moments with non-uniform orientation as indicated by the red and blue colors in the magnetic field maps, and thus do not cause the Fano resonance (Figure S22B-D, Supporting Information).

15214095, 2023, 33, Downloaded from https://onlinelibrary.wiley.com/doi/10.1002/adma.202301323 by University Of Pennsylvania, Wiley Online Library on [19/03/2024]. See the Terms and Conditions (https://onlinelibrary.wiley.com/emrs

nditions) on Wiley Online Library for rules of use; OA articles are governed by the applicable Creative Commons



templates with increasing  $S_t$ . B) The average interparticle gap,  $\overline{g1}$ , and the standard deviation in the interparticle gap,  $\sigma_{\rm g1}$ , between the central and the surrounding pentagonal NPs in the hexamer metamolecules plotted versus St. C) Dark-field scattering spectra and D) simulated scattering cross-sections of the metamolecules in (A), plotted with colors corresponding to the borders of the SEM images of the metamolecules. E) Simulated time snapshots of the z-component (normal to the sample) of the electric displacement maps, with electric displacement vectors in the x-y plane overlaid, at the wavelengths indicated by labels I, II, and III in (D); dipolar and quadrupolar charge distributions are labeled with 2 and 4, respectively. F) Ratio in intensities at Fano dip II and peak III, Idip/Ipeak (left axis), as well as the average interparticle gap,  $\overline{g1}$ , realized with templates of different  $S_t$  (right axis) versus the wavelength of the  $dip_{min}$ . G) SEM image of the pentagonal Au NP hexamer with 18° clockwise rotation and H) corresponding scattering spectra measured at angles of clockwise rotation. The radial direction is the wavelength, and polar angles are azimuthal angles of sample rotation, with illumination from the right. Measurements are taken in 18° increments, and values at intermediate angles are obtained through interpolation.

For pentagonal Au NP hexamers, larger g1 and thus weaker interparticle coupling lead to Fano dips with smaller modulation depths ( $I_{\rm dip}/I_{\rm peak}$  approaches 1), which is shown in Figure 5F (left axis), and at shorter wavelengths (right axis of Figure 5F). [53,54] However, the variation among metamolecules with the same  $S_{\rm t}$  value is large due to their different structural asymmetries. We performed a study on the polycyclic hexamer of pentagonal Au

NPs with smaller g1 (31 nm) and greater symmetry, shown in Figure 5G, in which we measured the dark-field scattering spectra at every 18° in rotation (Figure 5H). When the overall orientation of the metamolecule is preserved, we found that asymmetry of the center NP along the incident polarization and perpendicular to the propagation direction leads to a stronger interaction with the NP annulus and therefore, a larger modulation depth and a redder dip<sub>min</sub>.<sup>[55]</sup> In contrast, asymmetry along the propagation direction and perpendicular to the incident polarization flattens the modulation depth (Figure S23, Supporting Information). While five lobes of peak III are present in the inner circle of the azimuthal map, a deviation from perfect five-fold rotation symmetry is caused by the symmetry breaking discussed above. A more substantial modulation depth is obtained when two NPs on the right edge close to the excitation are aligned to the polarization direction, corresponding to the configuration represented in Figure 5G. In contrast, if two NPs on the left edge away from the excitation are aligned to the polarization direction, the modulation depth is lower. This is because more NPs on the right edge support stronger interaction with the incoming light incident from the right, in which case a hexapole charge distribution is created on the central NP at the resonance energy of the dip due to increased coupling strength (Figure S24, Supporting Information).

### 3. Conclusion

We report a fabrication process to produce NPs with well-defined sizes, shapes, and compositions, that are often not accessible synthetically, and assemble these NPs into open or close-packed NP metamolecules using a template-assisted assembly method. By engineering the size and shape of the NPs and of the templates, we create NP metamolecules with control over NP number and coordination, interparticle gap size and disorder, and the location of defects such as voids. Our results demonstrate that the occurrence and characteristics of Fano resonances in the scattering spectra can be systematically and precisely manipulated by controlling the coordination number, interparticle distance, symmetry, and orientation of the assembly relative to the propagation direction and incident polarization.

Our method offers several advantages over using only EBL techniques. The nanoimprint templates, fabricated with a single EBL exposure, are reusable. The feature size in the assembly templates is on the order of hundreds of nanometers, which is easy to achieve by EBL and could be realized by imprint lithography. The assembly process provides enhanced resolution, akin to pattern multiplication in block copolymer selfassembly,[56] as multiple NPs with tens of nanometer interparticle gaps are assembled in each trap, promising scalability over large device areas while maintaining fine features. The yield and precision of the assembly could be improved by exploiting the flexibility to tune the NP functionalization in the colloidal state, and further enhanced by adding funneled traps and auxiliary sidewalls in the assembly templates, as suggested by previous research.[18] Moreover, the functionalization of NPs with responsive ligands<sup>[57]</sup> and templates (e.g., Au) with other properties can introduce additional functionality to the assembled structure.[58]

1521495,2023, 33. Downloaded from https://onlinelibrary.wiley.com/do/i/0.1002/dma.20231323 by University of Pennsylvania, Wiley Online Library on [19/03/2024]. See the Terms and Conditions (https://onlinelibrary.viety.com/terms-and-conditions) on Wiley Online Library for rules of use; OA articles are governed by the applicable Cerative Commons and Conditions (https://onlinelibrary.viety.com/terms-and-conditions) on Wiley Online Library for rules of use; OA articles are governed by the applicable Cerative Commons and Conditions (https://onlinelibrary.viety.com/terms-and-conditions) on Wiley Online Library for rules of use; OA articles are governed by the applicable Cerative Commons and Conditions (https://onlinelibrary.viety.com/terms-and-conditions) on Wiley Online Library for rules of use; OA articles are governed by the applicable Cerative Commons and Conditions (https://onlinelibrary.viety.com/terms-and-conditions) on Wiley Online Library for rules of use; OA articles are governed by the applicable Cerative Commons and Conditions (https://onlinelibrary.viety.com/terms-and-conditions) on Wiley Online Library for rules of use; OA articles are governed by the applicable Cerative Commons and Conditions (https://onlinelibrary.viety.com/terms-and-conditions) on Wiley Online Library for rules of use; OA articles are governed by the applicable Cerative Commons and the conditions are governed by the applicable Cerative Commons and the conditions are governed by the applicable Cerative Commons are go

This work sets the stage to expand the fabrication and assembly of metamolecules composed of varying size and shape NPs, including NPs with the shape of irregular polygons and assemblies with more complex NP tilings. The integration of fabricated and chemically synthesized NPs expands the range of available materials.<sup>[59]</sup> Building on this report of "elemental" NP metamolecules and exploiting different sizes, shapes, and compositions of NPs, we are developing a multistep assembly method to realize heteroatomic, multimaterial, metamolecule architectures with mixed functions. [60] This approach eliminates the need for costly and time-consuming alignment EBL processes that require multiple exposures. For instance, cavities constructed from plasmonic metamolecules can control the luminescence intensities and lifetimes of emitters, making them useful for quantum information science when filled with single-photon emitters such as semiconductor quantum dots,[61] and for sensing and lasing when combined with up conversion NPs. [62,63] Plasmonic enhancement of semiconductor NP absorption can lead to more efficient and singlestructure photodetectors.<sup>[64]</sup> These techniques can be used to create miniaturized optoelectronic devices for emission and detection.

## 4. Experimental Section

Fabrication of Nanoimprint Molds: Nanoimprinting molds were fabricated using EBL. EBL resist ZEP-520A (1:1 diluted in anisole, Zeon Corporation) was deposited by spincoating at 3000 rpm for 1 min (total thickness was  $\approx \!133$  nm) onto device-grade Si wafers with a 250 nm SiO $_2$  layer and baked at 180 °C for 3 min. The resist layer was exposed in JEOL JBX-6300FS EBL writer operating at a 100 kV accelerating voltage and 1 nA beam current

After exposure, the wafer was developed in amyl acetate for 1 min and rinsed with isopropyl alcohol. Next, a 20 nm Cr layer was coated onto the patterned wafer using a Lesker PVD75 E-beam evaporator, followed by lift-off in Remover PG (MicroChem) at 80 °C for 2 h. The Cr hard mask was used to transfer the EBL pattern into the  $\mathrm{SiO}_2$  layer on the Si wafer using reactive ion etching (Oxford 80 plus RIE, 40 mTorr, Ar 38 sccm, CHF $_3$  12 sccm, 280 W) with an etch depth of  $\approx\!220$  nm. The Cr mask was removed by soaking in Cr etchant (Transene Company, Inc.) for 2 min and rinsing with water. Finally, the nanoimprinting mold was treated by an O $_2$  plasma (March Jupiter II, 68 sccm, 86 W, 15 min) and immediately soaked in a 1:1000 n-octadecyltrichlorosilane hexane solution for 10 min and rinsed with hexane and isopropyl alcohol.

Fabrication of NPs Using Nanoimprint Lithography: A Si wafer was sequentially coated with three layers of resists by spincoating. Durimide (Durimide 20–500, Fujifilm, 2000 rpm) and baking at 300 °C for 5 min, spincoating PMGI (SF5, Microchem, 2000 rpm) and baking at 180 °C for 3 min, and finally spincoating the thermal imprint resist (NXR-1025, 7%, Nanonex, 2000 rpm) and baking at 155 °C for 3 min.

The nanoimprint mold was imprinted into the thermal resist at 133 °C and 350 psi for 5 min and 30 s. The PMGI layer was exposed to an  $O_2$  plasma descum process (Oxford 80 plus RIE, 40 mTorr,  $O_2$  20 sccm, 100 W, 10 s) and developed in MF26A (Microchem, 15 s) to form the undercut structure. A thin film of Pd, Ge, or Au was deposited onto the patterned wafer using thermal evaporation (Lesker PVD75 E-beam/thermal Evaporator). The thin film on top of the thermal resist was lifted-off by immersion in acetone. The PMGI and Durimide resist layers were removed by  $O_2$  plasma (March Jupiter II, 68 sccm, 55 W, 3.75 min). Only the Durimide resist underneath and binding the NPs to the wafer remains

Fabricated NPs bonded to the wafer were soaked in solutions of a  $\omega$ -thiol-terminated PVP (1 mL, 0.5 mg mL $^{-1}$ , Mn = 1.5  $\times$  10 $^3$  g mol $^{-1}$ , Poly-

mer Source) in NMP (Sigma–Aldrich) for 18 h to both achieve PVP coating of the NPs and disperse the NPs in NMP. The NP dispersions were sonicated and then precipitated via centrifugation at 4000 rpm for 5 min. After removing the supernatant, the NPs were redispersed in DMF (0.5 mL, N,N-dimethylformamide, Sigma–Aldrich) and precipitated again by centrifugation. The above cleaning process was repeated with  $\rm H_2O$  (0.5 mL) three times to remove excess, unbound polymer ligands. Finally, the NPs were concentrated in a final  $\rm H_2O$  dispersion to  $\approx\!5~\mu L$  total volume to perform the template-assisted assembly.

Fabrication of Templates for Template-Assisted Capillary Self-Assembly: The templates for assembly were fabricated on double-side-polished Si wafers with a 280 nm SiO $_2$  layer grown by CVD (Oxford Instruments Plasma Lab 100 PECVD). Poly(methyl methacrylate) (PMMA) positive resist, 950k molecular weight (PMMA 950 A4, Kayaku) was deposited by spincoating onto the Si wafers at 6000 rpm for 1 min (total thickness  $\approx$  157 nm) and baked at 180 °C for 2 min. The resist layer was exposed in an Elionix ELS-7500EX EBL writer operating at 50 kV accelerating voltage and 50 pA beam current. The templates were developed in a 1:3 solution of MIBK:IPA for 90 s. An O $_2$  plasma descum (6 s, 75 W, 20 sccm, Gatan Solarus) was performed before the assembly process.

Template-Assisted Assembly: A home-built capillary assembly apparatus was used for the template-assisted assembly process. [25,26,43] A 5 μL, aqueous NP dispersion was added between the template and a glass slide. Then, a motorized linear stage (New Focus Picomotor) moves the template with a speed of 2 μm s $^{-1}$ . The substrate temperature during assembly was 22 °C, and the ambient dew point was kept at <-30 °C. After assembly, the PMMA template was lifted off by soaking in NMP for 1 min and acetone for 1 min.

Darkfield Scattering and Other Characterization of the Assembled Structures: A modified Olympus BX51 microscope was used for collecting the reflection-mode, dark-field scattering spectra of the assembled NP metamolecules with a NIR-optimized objective lens (Olympus LCPLN50XIR, NA 0.65). [25,26] The white light source was a 150-W quartz tungsten halogen lamp routed to the side of the microscope with an optical fiber bundle. A plano-convex lens collimates the light from the optical fiber bundle. The polarization of the incident light was selected with a rotatable broadband linear polarizer. Finally, another lens focuses the light onto the sample. The elevation angle of the incident light was  $\approx\!10^\circ$  above the horizontal. Incident and reflected light were avoided by the collection cone of the objective, forming a dark-field configuration. A 100-µmcore optical fiber spatially selects the scattering signal collected by the objective. The spectra were collected by a Princeton Instruments Tri-Vista 555 spectrometer equipped with a PIXIS-256E Si 2D array detector and an OMA-V InGaAs linear array detector for visible and NIR measurement. All scattering spectra were normalized by the spectrum of the incident light. Baseline subtraction was performed by removing the background scattering signal from a blank area on the substrate having no

SEM imaging of the structures was performed on FEI Quanta 600 FEG Mark II. TEM imaging was performed on a JEOL JEM-1400. AFM measurements were conducted on an Asylum Research MFP-3D-BIO AFM

Simulations: All the numerical computations were carried out in 3D finite element software, COMSOL MultiPhysics. The simulation setup was designed to imitate the experimental measurement setup as reported in the Experimental Section of darkfield scattering. NPs were illuminated by a plane wave with a 10° incident angle above the horizontal. All samples were surrounded by air and lying on a 280 nm  $SiO_2$  layer atop a Si wafer and were terminated by a perfectly matched layer. The permittivity of Au was from an analytical model reported in ref. [ $^{65}$ ]

$$\varepsilon_{Au} (\lambda) = \varepsilon_{\infty} - \frac{1}{\lambda_{p}^{2} (1/\lambda^{2} + i/\gamma_{p}\lambda)} + \sum_{i=1,2} \frac{A_{i}}{\lambda_{i}} \left[ \frac{e^{i\phi_{i}}}{(1/\lambda_{i} - 1/\lambda - i/\gamma_{i})} + \frac{e^{-i\phi_{i}}}{(1/\lambda_{i} + 1/\lambda + i/\gamma_{i})} \right]$$
(1)



www.advancedsciencenews.com

ADVANCED MATERIALS

www.advmat.de

where the high-frequency limit dielectric constant  $(\epsilon_{\infty})$  was 1.53, plasma wavelength  $(\lambda_{\rm p})$  and damping  $(\gamma_{\rm p})$  were 145 and 17 000 in nm, respectively; the parameters for the two interband transitions  $[A_i,\,\phi_i\,\,({\rm rad}),\,\lambda_i\,\,({\rm nm}),\,\gamma_i\,\,({\rm nm})]$  were 0.94,  $-\pi/4$ , 468, 2300 for i=1, and 1.36,  $-\pi/4$ , 331, 940 for i=2. The SEM image of each sample was imported into the software to set the geometry of NPs. The roughness of the NPs in simulations agrees with the experiments. The scattered electric  $(E_{\rm s})$  and magnetic fields  $(H_{\rm s})$  were computed numerically, and the scattering cross-section was calculated by integrating the Poynting vector over the same area as used in the experiments to collect the scattered field,  $\frac{1}{2}\int Re(E_{\rm s}\times H_{\rm s}^*).\hat{n}\,ds$  and normalized to the incident power density  $|E_{\rm o}|^2/2\eta_{\rm o}$ .

Statistical Analysis: In Figure 5B,F, the number of assemblies analyzed with  $S_t$  of 620, 650, and 670 nm were 12, 8, and 9, respectively. For each assembly, five interparticle distances were extracted from the SEM image. In Figure 5B, the error bars represent the mean  $\pm$  standard deviation (SD), while in Figure 5F, the box plots display the median, first, and third quartiles, as well as the minimum and maximum values. MATLAB was used for statistical analysis.

# **Supporting Information**

Supporting Information is available from the Wiley Online Library or from the author.

# Acknowledgements

The authors gratefully thank the Office of Naval Research Multidisciplinary University Research Initiative Award ONR N00014-18-1-2497 for primary support of the work, including NP nanofabrication and assembly and the structural and optical characterization of the NP metamolecules. Modifications of the microscope for angle-dependent scattering measurements and electron microscopy facilities were supported by the NSF MR-SEC program under Award No. DMR-1720530. The nanofabrication was conducted partially at the Singh Center for Nanotechnology, which was supported by the NSF National Nanotechnology Coordinated Infrastructure Program under grant NNCI-2025608. This research also used electron beam lithography infrastructure at the Center for Functional Nanomaterials (CFN), which was a U.S. Department of Energy Office of Science User Facility, at Brookhaven National Laboratory under Contract No. DE-SC0012704. The simulation effort was supported in part by the Defense Advanced Research Projects Agency (DARPA) Defense Sciences Office (DSO) Nascent Light-Matter Interaction Program under Grant No. W911NF-18-0369.

### **Conflict of Interest**

The authors declare no conflict of interest.

## **Data Availability Statement**

The data that support the findings of this study are available from the corresponding author upon reasonable request.

#### Keywords

Fano resonance, metamolecules, nanoparticle assemblies, optical magnetic resonance, plasmonics

Received: February 10, 2023 Revised: April 18, 2023 Published online: July 12, 2023

- L. Wang, M. H. Kafshgari, M. Meunier, Adv. Funct. Mater. 2020, 30, 2005400.
- [2] E. Roduner, Chem. Soc. Rev. 2006, 35, 583.
- [3] Y. Jun, J. Seo, J. Cheon, Acc. Chem. Res. 2008, 41, 179.
- [4] C. B. Murray, C. R. Kagan, M. G. Bawendi, Annu. Rev. Mater. Sci. 2000, 30, 545.
- [5] G. Haran, L. Chuntonov, Chem. Rev. 2018, 118, 5539.
- [6] X. Lu, M. Rycenga, S. E. Skrabalak, B. Wiley, Y. Xia, Annu. Rev. Phys. Chem. 2009, 60, 167.
- [7] M. A. Boles, M. Engel, D. V. Talapin, Chem. Rev. 2016, 116, 11220.
- [8] C. B. Murray, C. R. Kagan, M. G. Bawendi, Science 1995, 270, 1335
- [9] T. Vo, S. C. Glotzer, Proc. Natl. Acad. Sci. USA 2022, 119, e2116414119.
- [10] W. Zhou, Z. Liu, Z. Huang, H. Lin, D. Samanta, Q.-Y. Lin, K. Aydin, C. A. Mirkin, Proc. Natl. Acad. Sci. USA 2020, 117, 21052.
- [11] A. Biswas, I. S. Bayer, A. S. Biris, T. Wang, E. Dervishi, F. Faupel, Adv. Colloid Interface Sci. 2012, 170, 2.
- [12] J. Xu, D. H. C. Wong, J. D. Byrne, K. Chen, C. Bowerman, J. M. DeSimone, Angew. Chem., Int. Ed. 2013, 52, 6580.
- [13] W.-B. Jung, S. Jang, S.-Y. Cho, H.-J. Jeon, H.-T. Jung, Adv. Mater. 2020, 32, 1907101.
- [14] H. Duan, H. Hu, K. Kumar, Z. Shen, J. K. W. Yang, ACS Nano 2011, 5, 7593.
- [15] D. Samanta, W. Zhou, S. B. Ebrahimi, S. H. Petrosko, C. A. Mirkin, Adv. Mater. 2022, 34, 2107875.
- [16] C. Yi, H. Liu, S. Zhang, Y. Yang, Y. Zhang, Z. Lu, E. Kumacheva, Z. Nie, Science 2020, 369, 1369.
- [17] Z. Chai, A. Childress, A. A. Busnaina, ACS Nano 2022, 16, 17641.
- [18] V. Flauraud, M. Mastrangeli, G. D. Bernasconi, J. Butet, D. T. L. Alexander, E. Shahrabi, O. J. F. Martin, J. Brugger, *Nat. Nanotechnol.* 2017, 12, 73.
- [19] M. Grzelczak, J. Vermant, E. M. Furst, L. M. Liz-Marzán, ACS Nano 2010. 4, 3591.
- [20] Y. Xia, Y. Yin, Y. Lu, J. McLellan, Adv. Funct. Mater. 2003, 13, 907.
- [21] H. Zhang, Y. Liu, A. Ashokan, C. Gao, Y. Dong, C. Kinnear, N. Kirkwood, S. Zaman, F. Maasoumi, T. D. James, A. Widmer-Cooper, A. Roberts, P. Mulvaney, Adv. Opt. Mater. 2022, 10, 2200179.
- [22] L. Scarabelli, D. Vila-Liarte, A. Mihi, L. M. Liz-Marzán, Acc. Mater. Res. 2021, 2, 816.
- [23] T. Kraus, L. Malaquin, H. Schmid, W. Riess, N. D. Spencer, H. Wolf, Nat. Nanotechnol. 2007, 2, 570.
- [24] S. Ni, J. Leemann, H. Wolf, L. Isa, Faraday Discuss. 2015, 181, 225.
- [25] N. J. Greybush, I. Liberal, L. Malassis, J. M. Kikkawa, N. Engheta, C. B. Murray, C. R. Kagan, ACS Nano 2017, 11, 2917.
- [26] N. J. Greybush, V. Pacheco-Peña, N. Engheta, C. B. Murray, C. R. Kagan, ACS Nano 2019, 13, 3875.
- [27] L. S. Slaughter, B. A. Willingham, W.-S. Chang, M. H. Chester, N. Ogden, S. Link, Nano Lett. 2012, 12, 3967.
- [28] C. Matricardi, C. Hanske, J. L. Garcia-Pomar, J. Langer, A. Mihi, L. M. Liz-Marzán, ACS Nano 2018, 12, 8531.
- [29] Y. Cui, M. T. Björk, J. A. Liddle, C. Sönnichsen, B. Boussert, A. P. Alivisatos, Nano Lett. 2004, 4, 1093.
- [30] J. Henzie, S. C. Andrews, X. Y. Ling, Z. Li, P. Yang, Proc. Natl. Acad. Sci. USA 2013, 110, 6640.
- [31] T. D. Clark, J. Tien, D. C. Duffy, K. E. Paul, G. M. Whitesides, J. Am. Chem. Soc. 2001, 123, 7677.
- [32] T. D. Clark, R. Ferrigno, J. Tien, K. E. Paul, G. M. Whitesides, J. Am. Chem. Soc. 2002, 124, 5419.
- [33] A. Alù, N. Engheta, Phys. Rev. B 2008, 78, 85112.
- [34] S. N. Sheikholeslami, A. García-Etxarri, J. A. Dionne, Nano Lett. 2011, 11, 3927.

- [35] C. Cherqui, Y. Wu, G. Li, S. C. Quillin, J. A. Busche, N. Thakkar, C. A. West, N. P. Montoni, P. D. Rack, J. P. Camden, D. J. Masiello, *Nano Lett.* 2016, 16, 6668.
- [36] F. Shafiei, F. Monticone, K. Q. Le, X.-X. Liu, T. Hartsfield, A. Alù, X. Li, Nat. Nanotechnol. 2013, 8, 95.
- [37] N. Liu, S. Mukherjee, K. Bao, L. V. Brown, J. Dorfmüller, P. Nordlander, N. J. Halas, Nano Lett. 2012, 12, 364.
- [38] W. Hu, M. Zhang, R. J. Wilson, A. L. Koh, J. S. Wi, M. Tang, R. Sinclair, S. X. Wang, *Nanotechnology* 2011, 22, 185302.
- [39] M.-C. Daniel, D. Astruc, Chem. Rev. 2004, 104, 293.
- [40] R. Lück, Mater. Sci. Eng., A 2000, 294-296, 263.
- [41] S. Ni, L. Isa, H. Wolf, Soft Matter 2018, 14, 2978.
- [42] M. J. Gordon, D. Peyrade, Appl. Phys. Lett. 2006, 89, 053112.
- [43] H. J. Shulevitz, T.-Y. Huang, J. Xu, S. J. Neuhaus, R. N. Patel, Y. C. Choi, L. C. Bassett, C. R. Kagan, ACS Nano 2022, 16, 1847.
- [44] E. Ringe, M. R. Langille, K. Sohn, J. Zhang, J. Huang, C. A. Mirkin, R. P. Van Duyne, L. D. Marks, J. Phys. Chem. Lett. 2012, 3, 1479.
- [45] P. Wang, J.-H. Huh, J. Lee, K. Kim, K. J. Park, S. Lee, Y. Ke, Adv. Mater. 2019, 31, 1901364.
- [46] J. A. Fan, C. Wu, K. Bao, J. Bao, R. Bardhan, N. J. Halas, V. N. Manoharan, P. Nordlander, G. Shvets, F. Capasso, *Science* 2010, 328, 1135.
- [47] https://www.comsol.com/.
- [48] A. Alù, A. Salandrino, N. Engheta, Opt. Express 2006, 14, 1557.
- [49] J. A. Fan, Y. He, K. Bao, C. Wu, J. Bao, N. B. Schade, V. N. Manoharan, G. Shvets, P. Nordlander, D. R. Liu, F. Capasso, *Nano Lett.* 2011, 11, 4859.
- [50] J. A. Fan, K. Bao, J. B. Lassiter, J. Bao, N. J. Halas, P. Nordlander, F. Capasso, *Nano Lett.* 2012, 12, 2817.
- [51] F. Tam, A. L. Chen, J. Kundu, H. Wang, N. J. Halas, J. Chem. Phys. 2007, 127, 204703.

- [52] L.-Y. Yin, Y.-H. Huang, X. Wang, S.-T. Ning, S.-D. Liu, AIP Adv. 2014, 4, 77113.
- [53] M. Hentschel, M. Saliba, R. Vogelgesang, H. Giessen, A. P. Alivisatos, N. Liu, A. P. Alivisatos, N. Liu, Nano Lett. 2010, 10, 2721.
- [54] A. Lovera, B. Gallinet, P. Nordlander, O. J. F. Martin, ACS Nano 2013, 7, 4527.
- [55] N. A. Mirin, K. Bao, P. Nordlander, J. Phys. Chem. A 2009, 113, 4028
- [56] S.-J. Jeong, J. Y. Kim, B. H. Kim, H.-S. Moon, S. O. Kim, Mater. Today 2013, 16, 468.
- [57] M. Grzelczak, L. M. Liz-Marzán, R. Klajn, Chem. Soc. Rev. 2019, 48, 1342.
- [58] M. Saboktakin, X. Ye, S. J. Oh, S.-H. Hong, A. T. Fafarman, U. K. Chettiar, N. Engheta, C. B. Murray, C. R. Kagan, ACS Nano 2012, 6, 8758.
- [59] Y.-Y. Cai, Y. C. Choi, C. R. Kagan, Adv. Mater. 2022, 2108104.
- [60] M. Zhang, D. J. Magagnosc, I. Liberal, Y. Yu, H. Yun, H. Yang, Y. Wu, J. Guo, W. Chen, Y. J. Shin, A. Stein, J. M. Kikkawa, N. Engheta, D. S. Gianola, C. B. Murray, C. R. Kagan, Nat. Nanotechnol. 2017, 12, 228.
- [61] H. A. Nguyen, D. Sharp, J. E. Fröch, Y.-Y. Cai, S. Wu, M. Monahan, C. Munley, A. Manna, A. Majumdar, C. R. Kagan, B. M. Cossairt, ACS Appl. Mater. Interfaces 2023, 15, 4294.
- [62] N. J. Greybush, M. Saboktakin, X. Ye, C. Della Giovampaola, S. Ju Oh, N. E. Berry, N. Engheta, C. B. Murray, C. R. Kagan, ACS Nano 2014, 8, 9482.
- [63] Y. Meng, D. Huang, H. Li, X. Feng, F. Li, Q. Liang, T. Ma, J. Han, J. Tang, G. Chen, X.-W. Chen, *Nat. Photonics* 2023, 17, 73.
- [64] M. Dai, H. Chen, R. Feng, W. Feng, Y. Hu, H. Yang, G. Liu, X. Chen, J. Zhang, C.-Y. Xu, P. Hu, ACS Nano 2018, 12, 8739.
- [65] P. G. Etchegoin, E. C. Le Ru, M. Meyer, J. Chem. Phys. 2006, 125, 164705